



## 2D Janus and non-Janus diamanes with an in-plane negative Poisson's ratio for energy applications



Deobrat Singh <sup>a,\*</sup>, Nabil Khossossi <sup>a,1</sup>, Wei Luo <sup>a</sup>, Abdelmajid Ainane <sup>b</sup>, Rajeev Ahuja <sup>a,c,\*\*</sup>

<sup>a</sup> Condensed Matter Theory Group, Materials Theory Division, Department of Physics and Astronomy, Uppsala University, Box 516, 75120, Uppsala, Sweden

<sup>b</sup> Laboratoire de Physique des Matériaux et Modélisations des Systèmes, (LP2MS), Faculty of Sciences, Department of Physics, Moulay Ismail University, Meknes, Morocco

<sup>c</sup> Department of Physics, Indian Institute of Technology Ropar, Rupnagar, 140001, Punjab, India

### ARTICLE INFO

#### Article history:

Received 30 December 2021

Received in revised form

15 February 2022

Accepted 15 February 2022

### ABSTRACT

Motivated by the successful synthesis of 2D C<sub>2</sub>F diamanes [Bakharev, P.V. et al., Nat. Nanotechnol. 15, 59–66 (2020)], we have systematically investigated the structural stability, in-plane mechanical, optoelectronic, photocatalytic, piezoelectric, and thermoelectric properties of non-Janus and Janus diamanes monolayers named as C<sub>2</sub>H, C<sub>2</sub>F, C<sub>2</sub>Cl, C<sub>4</sub>HF, C<sub>4</sub>HCl and C<sub>4</sub>FCl. The structural stability is confirmed by cohesive energy, phonon dispersion spectra, and mechanical properties. The electronic properties has been calculated by HSE06 functional and the band gap are found to be 3.85, 5.64, 2.32, 4.16, 0.73 and 1.91 eV for C<sub>2</sub>H, C<sub>2</sub>F, C<sub>2</sub>Cl, C<sub>4</sub>HF, C<sub>4</sub>HCl and C<sub>4</sub>FCl, respectively. The hydrogen-containing non-Janus and Janus diamanes monolayers have a higher negative Poisson's ratio (NPR) and therefore are good auxetic materials. From the Poisson's ratio and Young's modulus of each configuration of non-Janus and Janus diamanes monolayer, anisotropic behavior was displayed. From the optical properties calculations, the refractive index values are around 1.5, which means that it will be a transparent monolayered materials. Also, C<sub>2</sub>Cl, C<sub>4</sub>HCl and C<sub>4</sub>FCl monolayers displayed high absorption spectra with an order of 10<sup>5</sup> cm<sup>-1</sup> in the visible region, which shows great applications in optoelectronic devices. Additionally, the valence and conduction band-edge positions of 2D Janus and non-Janus diamanes of C<sub>2</sub>H, C<sub>2</sub>F, and C<sub>2</sub>Cl and C<sub>4</sub>HF monolayers have to straddle the redox potentials of water. It means that the photogenerated electrons and holes are sufficient to drive the overall water splitting. Whereas non-Janus diamanes C<sub>4</sub>HCl, and C<sub>4</sub>FCl monolayers displayed only water oxidation. The investigated in-plane piezoelectric coefficient has larger in non-Janus diamanes C<sub>4</sub>HF, C<sub>4</sub>HCl, and C<sub>4</sub>FCl monolayers. Therefore, it is very useful in the field of piezoelectric applications. From the thermoelectric properties, the non-Janus and Janus diamanes monolayers have great thermoelectric efficiency and were found to be 10.52 and 10.63% for C<sub>2</sub>H and C<sub>2</sub>F, respectively. Our results demonstrate the new class of 2D carbon-based monolayers has good auxetic materials as well as a wide range of applications in optoelectronics, piezoelectric, and thermoelectric fields.

© 2022 The Authors. Published by Elsevier Ltd. This is an open access article under the CC BY license (<http://creativecommons.org/licenses/by/4.0/>).

### 1. Introduction

Currently, two-dimensional (2D) based materials represent one of the more exciting and dynamic categories of materials, which are constantly growing rapidly through computational screening and/or experimental predictions as well as the design of new structures. The first excitement surrounding 2D materials was boosted following the outstanding and successful isolation of single-layer graphene in 2004 [1,2]. In the wake of the landmark achievements of graphene monolayer, the 2D carbon-based frameworks

\* Corresponding author.

\*\* Corresponding author. Condensed Matter Theory Group, Materials Theory Division, Department of Physics and Astronomy, Uppsala University, Box 516, 75120, Uppsala, Sweden.

E-mail addresses: [deobrat.singh@physics.uu.se](mailto:deobrat.singh@physics.uu.se) (D. Singh), [rajeev.ahuja@physics.uu.se](mailto:rajeev.ahuja@physics.uu.se) (R. Ahuja).

<sup>1</sup> DS and NK have equally contributed in this research article. WL, AA, and RA has helped to improve the scientific content of the research article. RA has conceptualized, supervised, facilitated resources and funding for this work.

with planar and non-planar structures have become the focus of considerable scrutiny. Out of diverse graphene homologues, hexagonal graphene-like structure like boron nitride (h-BN) [3], Boron phosphide (h-BP) [4,5], Boron Arsenide (h-BAs) [6] and Germanium-graphene (g-GeC) [7], 2D Janus monolayers and bilayers of group IV transition-metal mono/bi/tri-chalcogenides and so on [8–20], and MXenes [21,22] have been thoroughly probed over the recent decades. The key strength of these mentioned 2D materials over the pristine graphene monolayer consists of their underlying semiconducting electronic character, while the Dirac cone and zero electronic band gap nature of the pristine graphene restrict its applicability towards a variety of electronic devices. It is noteworthy that exhibiting a semiconducting electronic characteristic with a suitable band gap value is a key requirement for a wide range of applications, including nano-electronics, optoelectronics, sensors, and photocatalysis [14,23–26].

However, over the past few years, a considerable effort has been made to develop and explore new 2D carbon-based materials with semiconducting behavior. In this context, 2D frameworks based on covalently bonded C- and N-atoms have generated significant interest as part of a new family of 2D carbon-based materials featuring semiconducting characteristics that are appropriate for a variety of multi-functional devices. First, 2D g-C<sub>3</sub>N<sub>4</sub> monolayer have been successfully synthesized over an extended time by various processes and have demonstrated a narrow electronic bandgap with outstanding chemical and physical properties to be used for energy-based technologies including batteries, photocatalysis, sensors, and so on [27–32]. Based on the outstanding performance achieved by 2D g-C<sub>3</sub>N<sub>4</sub> monolayer, a variety of other 2D carbon-nitride based materials (e.g., C<sub>2</sub>N, C<sub>3</sub>N, C<sub>3</sub>N<sub>3</sub> and C<sub>3</sub>N<sub>5</sub> monolayers) [33–37] have been successfully conceptualized and synthesized experimentally over the past few years. All these breakthroughs underline the outstanding perspectives in the prediction and development of new carbon-based 2D materials with a semiconducting nature.

Many experimental and theoretical efforts have been made towards opening the band gap of graphene to achieve semiconducting characteristics [38–44], namely hydrogenation/florination of pristine graphene [45,46], cutting graphene monolayer into nanoribbons [47,48], induced by patterned hydrogen adsorption [49] and graphene substrate interaction [40,50,51]. Nevertheless, all of such techniques significantly decrease the carrier mobility or open only a finite electronic bandgap because of the distortion of the hexagonal lattice and strict conditions on the surface quality of the material. More recently, a new strategy which is based on the transformation of multilayer graphene into diamane nanomembranes referred to as “diamane”, has been reported theoretically and successfully synthesized [52–55]. Therefore, to realize this transformation successfully and hold the geometrical, energetic, thermodynamic, and mechanical stability of the diamane monolayer in the operating environment, the external surfaces of the pristine graphene monolayer need to be functionalized by fluorine (-F), hydrogen (-H) or hydroxyl group (-OH). The hybridization occurring at the sp<sup>3</sup> and dz<sup>2</sup> orbitals is thought to be the principal motivating interaction behind the transformation of multilayer graphene to diamane monolayers [56–58]. In particular, a lot of experimental efforts have been made to properly synthesize this new class of 2D materials. First, fluorographene and hydrographene have been successfully synthesized experimentally [59,60]. Also, the recent progress made in the growth of graphene through Chemical-Vapor-Deposition (CVD) has provided directions for converting multilayer graphene to “diamane” sheets [61–63].

Driven by the aforementioned theoretical and experimental achievements in these new 2D materials, we investigate the structural, energetic, mechanical, and thermodynamic stability of

2D Janus and non-Janus diamanes made of fluorinated, hydrogenated, and chlorinated graphene monolayers. Then, the in-plane mechanical, electronic, and optical properties and other multi-functional properties of these materials are studied through the first principle-based density functional theory and the Boltzmann transport-based equation. Our research offers an in-depth understanding of the physical behavior of these 2D Janus and non-Janus diamanes materials towards task-specific applications, including optoelectronics, photocatalysis, piezoelectric, and thermoelectric devices, and also provides suitable directions for the development and processing of these new 2D carbon-based materials.

## 2. Computational details

In this work, structural, optoelectronic, and photocatalytic properties were explored based on Density Functional Theory (DFT) as part of the Vienna Ab Initio Simulation Package (VASP) [64] code. The standard Generalized-Gradient-Approximation in the form of Perdew Burke Ernzerhof (GGA-PBE) functional [65] is implemented self consistently within the framework of the Projector Augmented Wave using the plane-wave basis ensemble with a kinetic-energy cutoff of about 600 eV and the convergence criteria during the geometry optimizations were set to 10<sup>-6</sup> eV and 10<sup>-4</sup> eV/Å for energy and force, respectively. Furthermore, for a better understanding of electronic trend and derived an accurate band gap value of our materials, the Heyd Scuseria Ernzerhof (HSE06) exchange-correlation hybrid functional were employed with a mixing parameter of about 25% [66]. During the geometry optimization of all structures, the vacuum layer was set to 20 Å in the c-direction in order to avoid the interaction between stacked layers and periodic pictures. The Monkhorst Pack K-point of 24×24×1 grid is used in the reciprocal space during the geometrical optimizations [67]. The charge transfer between atoms is evaluated on the basis of the Bader charge algorithm [68]. For the purpose of re-checking the thermodynamic stability of the free-standing structures obtained after full optimization, the force constants are obtained by using the finite displacement approach as implemented in Phonopy package [69–71]. Moreover, to check the thermal stability, we perform the ab initio molecular dynamics (AIMD) simulations in the NVT ensemble with a time step of 2 fs for 10 ps at 1000 K [72,73]. The lattice part of thermal conductivity has been calculated by using ShengBTE code [74] and the thermoelectric properties have been investigated by BoltzTraP code [75].

## 3. Results and discussion

### 3.1. Geometry and structural stability

The full optimized structures of the non-Janus and Janus monolayers are presented in Fig. 1. Fig. 1a–c are the non-Janus structures functionalized with H, F, and Cl atoms on both sides of the C atoms. Table 1 displays the lattice parameters and bond length between the C–C, C–H, C–Cl, and C–F in non-Janus and Janus monolayers, which is in excellent agreement with previous work [76].

Furthermore, we have investigated the phonon dispersion spectra to check the dynamical stability of these Janus and non-Janus diamanes monolayers. The phonon dispersion spectra are presented in Fig. 2. Due to the presence of all positive frequency modes in the entire Brillouin zone, the Janus and non-Janus diamanes monolayers displayed dynamical stability. Fig. S1 (see Supplementary Material (SM)) shows the contribution of partial phonon density of states. The vibration states of the lower atomic mass of atoms shifted to a lower phonon frequency side, and lighter atomic mass appeared on the higher phonon frequency side.

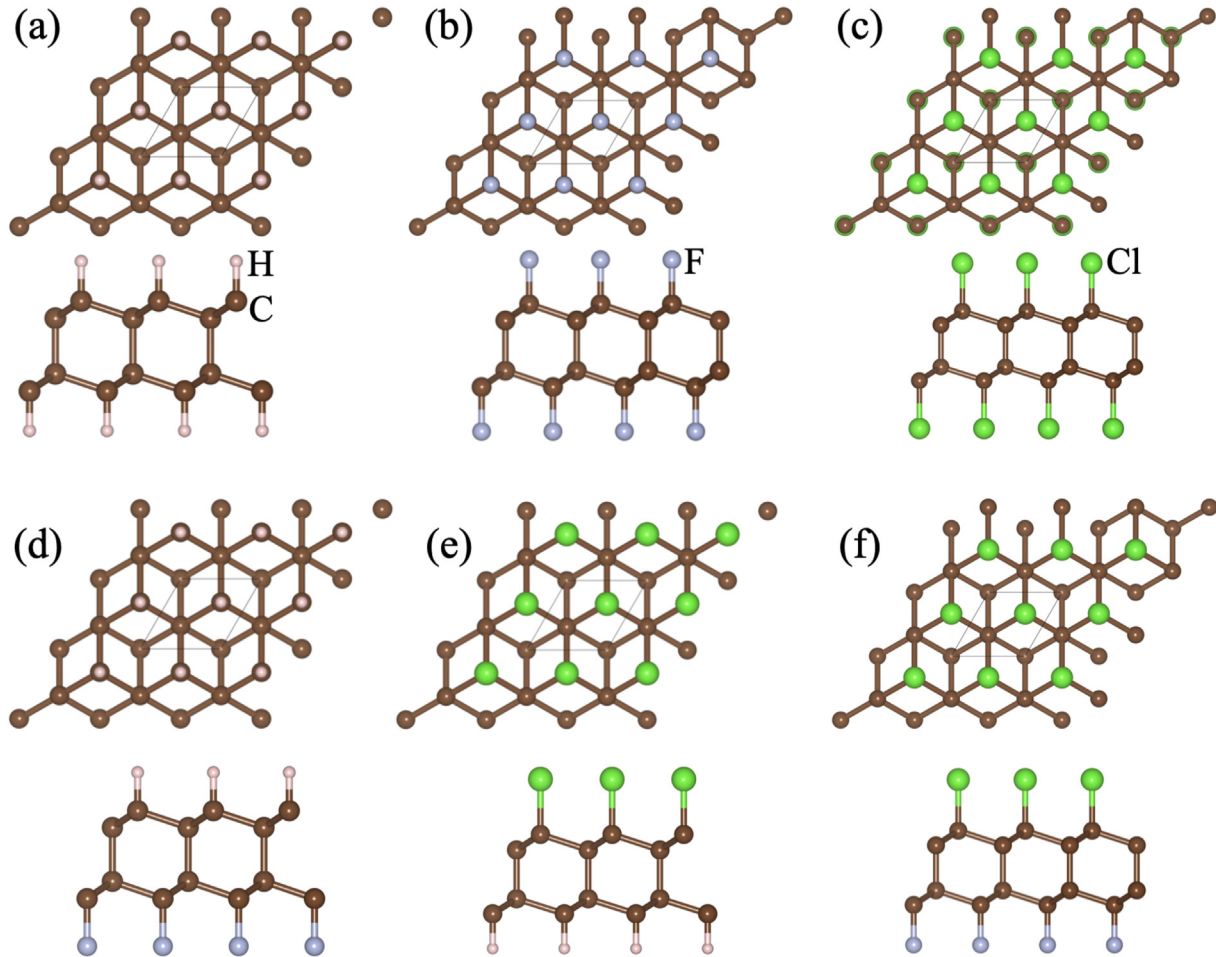


**Fig. 1.** Top and side view of freestanding Janus and non-Janus diamanes of (a) C<sub>2</sub>H, (b) C<sub>2</sub>F, (c) C<sub>2</sub>Cl, (d) C<sub>4</sub>HF, (e) C<sub>4</sub>HCl and (f) C<sub>4</sub>FCI monolayers with the unit cell indicated by a black hexagonal.

**Table 1**

Calculated lattice parameters ( $\text{\AA}$ ), bond lengths ( $\text{\AA}$ ) between C–C, C–H, C–Cl and C–F and cohesive energy (eV) in non-Janus and Janus monolayers.

System	a(=b)(\AA)	C–C(\AA)	C–H/C–F/C–Cl(\AA)	$E_{coh}$ (eV)
C <sub>2</sub> H	2.52	1.53–1.56	1.11	7.24
C <sub>2</sub> F	2.55	1.55	1.37	7.18
C <sub>2</sub> Cl	2.73	1.66	1.75	5.98
C <sub>4</sub> HF	2.53	1.55	1.11, 1.38	7.21
C <sub>4</sub> HCl	2.64	1.60	1.11, 1.76	6.55
C <sub>4</sub> FCI	2.65	1.61	1.37, 1.75	6.54

Additionally, to check the thermal stability, we have calculated the AIMD calculations at 1000 K for 10 ps. Fig. S2 and Fig. S3 (see in SM) represent the variation of the total energy of the system vs. time for non-Janus and Janus diamanes monolayers, respectively. There is less energy fluctuation and no breaking of bonds, which shows a high degree of stability. It means that non-Janus and Janus diamanes monolayers displayed thermal stability.

Also to check the energetically stable, we have calculated the cohesive energy of the on-Janus and Janus diamanes monolayer using following relation,

$$E_{coh} = \frac{n_1 E_C + n_2 E_X + n_3 E_Y - E_{C_XY}}{n_1 + n_2 + n_3} \quad (1)$$

where  $E_C$ ,  $E_X$ ,  $E_Y$  and  $E_{C_XY}$  are the total energy of single C atom,

single X atom, single Y atom and C<sub>2</sub>XY compound, respectively. And  $n_1$ ,  $n_2$  and  $n_3$  represent the number of C, X and Y atom present in the unit cell. The calculated non-Janus and Janus diamanes monolayers are presented in Table 1. The range of cohesive energy of the considered monolayer are found to be 5.98–7.24 eV/atom which is very near to the pristine graphene monolayer (9.16 eV/atom) and other carbon-related materials such as BC<sub>4</sub>N (8.93 eV/atom), and BCN (8.61 eV/atom) [77,78]. Such types of larger cohesive energy materials suggest that these monolayers have high energetic stability and mechanical strength [79].

### 3.2. Mechanical properties

In the present section, we discuss the mechanical properties to check the stability of Janus diamanes and Non-Janus diamanes systems. Also, we have calculated the in-plane Young's modulus and Poisson ratio along with different  $\theta$  directions relative to the positive x-direction as follows [80].

$$E(\theta) = \frac{C_{11}C_{22} - C_{12}^2}{C_{11}\sin^4\theta + C_{22}\cos^4\theta\left(\frac{C_{11}C_{22} - C_{12}^2}{C_{44}} - 2C_{12}\right)\cos^2\theta\sin^2\theta} \quad (2)$$

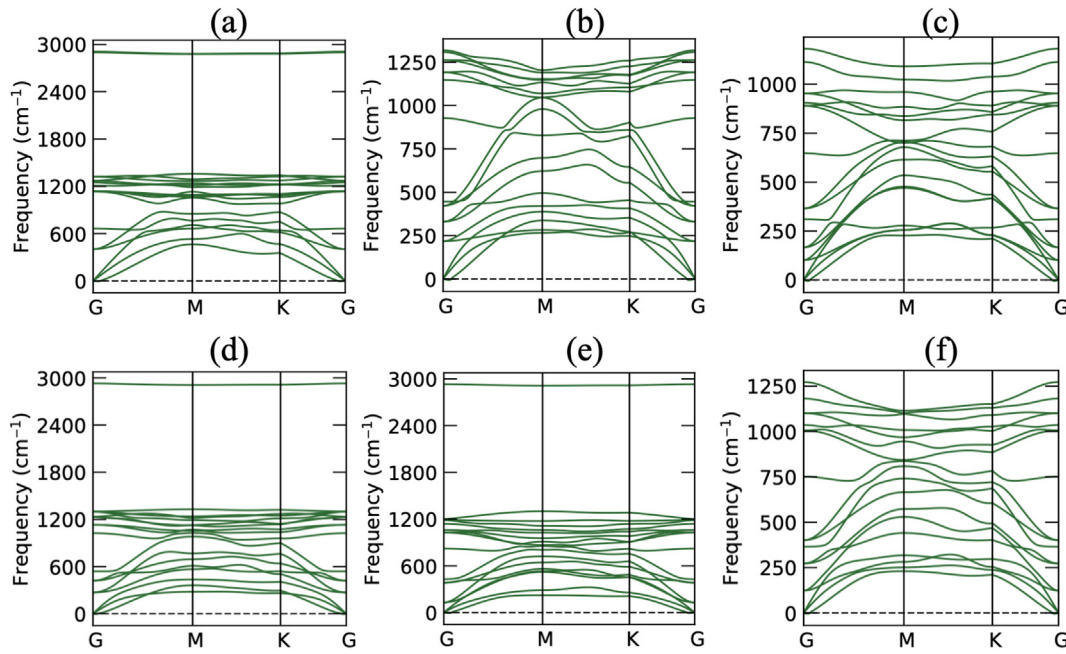


**Fig. 2.** Phonon band structures of Janus and non-Janus diamanes of (a) C<sub>2</sub>H, (b) C<sub>2</sub>F, (c) C<sub>2</sub>Cl, (d) C<sub>4</sub>HF, (e) C<sub>4</sub>HCl and (d) C<sub>4</sub>FCI monolayers.

$$\nu(\theta) = \frac{\left(C_{11} + C_{22} - \frac{C_{11}C_{22} - C_{12}^2}{C_{44}}\right)\cos^2\theta\sin^2\theta - C_{12}(\cos^4\theta + \sin^4\theta)}{C_{11}\sin^4\theta + C_{22}\cos^4\theta + \left(\frac{C_{11}C_{22} - C_{12}^2}{C_{44}} - 2C_{12}\right)\cos^2\theta\sin^2\theta} \quad (3)$$

The calculated elastic stiffness constants values of C<sub>11</sub>, C<sub>12</sub>, C<sub>22</sub>, C<sub>66</sub> are presented in Table S1 (see in SM), satisfy the necessary mechanical equilibrium conditions [81] of Born-Huang elastic criteria for mechanical stability: C<sub>11</sub>C<sub>22</sub>-C<sub>12</sub><sup>2</sup>>0 and C<sub>11</sub>, C<sub>22</sub>, C<sub>66</sub>>0. From Table S1 (see in SM), these considered systems satisfied the mechanical stability conditions. It means that the Janus diamanes and Non-Janus diamanes systems are mechanically stable. Further to the understanding of mechanical properties, we have calculated the orientation-dependent Young's modulus E(θ), Poisson's ratio ν(θ) and shear modulus G(θ) as shown in Fig. S4 (see in SM), Fig. 3 and Fig. S5 (see in SM). The orientation-dependent profile displays that the Young's modulus of Janus and Non-Janus diamanes monolayers is highly anisotropic behavior (see Fig. S4 in SM). The maximum values of Young's modulus along x-directions are 264 GPa, 276 GPa, 224 GPa, 262 GPa, 240 GPa and 249 GPa for C<sub>2</sub>H, C<sub>2</sub>F, C<sub>2</sub>Cl, C<sub>4</sub>HF, C<sub>4</sub>HCl and C<sub>4</sub>FCI monolayers, respectively. Whereas, its values along the y-directions are found to be 470 GPa, 500 GPa, 400 GPa, 466 GPa, 430 GPa, and 450 GPa for C<sub>2</sub>H, C<sub>2</sub>F, C<sub>2</sub>Cl, C<sub>4</sub>HF, C<sub>4</sub>HCl and C<sub>4</sub>FCI monolayers, respectively. It was seen that the minimal and maximal Young's modulus of the Janus and Non-Janus diamanes monolayers are almost very close to each other. It is clear that the Young's modulus values of the considered Janus and Non-Janus diamanes monolayers are smaller than graphene (1000 GPa) [82] while larger than phosphorene (166 GPa) [83], BN (250 GPa) [84] and MoS<sub>2</sub> (330 GPa) [85].

As shown in Fig. 3 displayed spatially varying the Poisson's ratio for C<sub>2</sub>H, C<sub>2</sub>F, C<sub>2</sub>Cl, C<sub>4</sub>HF, C<sub>4</sub>HCl and C<sub>4</sub>FCI monolayers. In particular, all the Janus and non-Janus diamanes monolayers displayed a negative Poisson's ratio along the 45° and 135° whereas the values of Poisson's ratio along the x- and y-directions are positive and relatively higher than negative values (see Fig. 3). The maximal negative values of Poisson's ratios are found to

be -0.071, -0.042, -0.0065, -0.058, -0.064 and -0.030 for C<sub>2</sub>H, C<sub>2</sub>F, C<sub>2</sub>Cl, C<sub>4</sub>HF, C<sub>4</sub>HCl and C<sub>4</sub>FCI monolayers, respectively. It was seen that the negative Poisson ratio is relatively higher than some of the reported 2D auxetic materials, such as penta-graphene (-0.07) [86], single-layer black phosphorus (-0.03) [87], borophene (-0.04) [88] and Penta-B<sub>2</sub>N<sub>4</sub> (-0.02) [89]. Apart from this, the maximal Poisson ratios are 0.13, 0.168, 0.22, 0.146, 0.13 and 0.183 along the y-direction, while in the x-direction, its values are relatively lower and found to be 0.07, 0.092, 0.12, 0.08, 0.075 and 0.105 for C<sub>2</sub>H, C<sub>2</sub>F, C<sub>2</sub>Cl, C<sub>4</sub>HF, C<sub>4</sub>HCl and C<sub>4</sub>FCI monolayers, respectively. It was noticed that the maximal negative/positive Poisson ratios are found in the case of C<sub>2</sub>H and C<sub>2</sub>Cl monolayers, respectively. Such types of auxetic materials (i.e. negative Poisson ratio materials) are very useful in various fields such as tougher composites, defense, medicine, and fasteners.

Additionally, we have investigated the Shear modulus of Janus and non-Janus diamanes monolayers in the xy-plane as shown in Fig. S5 (see in SM). It can be noticed that the Shear modulus is highly isotropic along x- and y-directions. The maximal Shear modulus values are 225, 230, 171, 220, 188 and 192 GPa for C<sub>2</sub>H, C<sub>2</sub>F, C<sub>2</sub>Cl, C<sub>4</sub>HF, C<sub>4</sub>HCl and C<sub>4</sub>FCI monolayers, respectively. The finding values of Shear modulus are larger than previously reported some of the 2D monolayered materials [80,90,91]. It means that the considered 2D monolayered materials are rigid.

### 3.3. Electronic properties

In the present section, we have calculated the electronic properties to understand the behaviors of 2D monolayer materials. Fig. 4 shows the orbital contributed electronic band structures of Janus and non-Janus diamanes monolayers. The 2D Janus and non-Janus diamanes monolayers show a direct band gap at G-point (see Fig. 4) which is well consistent with previously reported work [76]. The calculated band gap using PBE functional shows the band gap of 3.57, 3.92, 1.04, 0.25 and 0.71 eV for C<sub>2</sub>H, C<sub>2</sub>F, C<sub>2</sub>Cl, C<sub>4</sub>HF, C<sub>2</sub>HCl and C<sub>2</sub>FCI monolayers, respectively. Moreover, to find a more accurate electronic band gap, we have used hybrid functional HSE06 and the corresponding electronic band gaps of respective monolayer

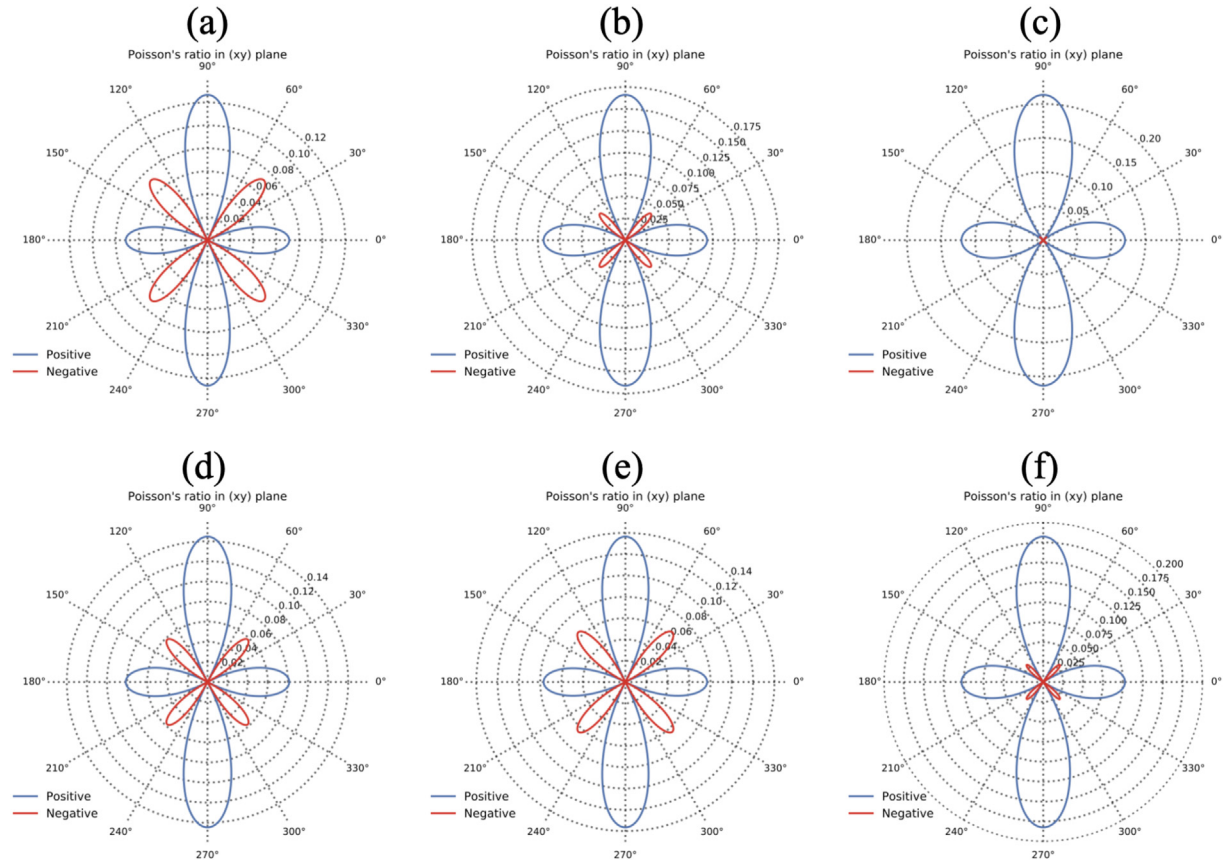


**Fig. 3.** Poisson's ratio of Janus and non-Janus diamanes of (a)  $\text{C}_2\text{H}$ , (b)  $\text{C}_2\text{F}$ , (c)  $\text{C}_2\text{Cl}$ , (d)  $\text{C}_4\text{HF}$ , (e)  $\text{C}_4\text{HCl}$  and (d)  $\text{C}_4\text{FCl}$  monolayers along  $xy$ -plane. The blue and red color represents the positive and negative Poisson's ratio, respectively.

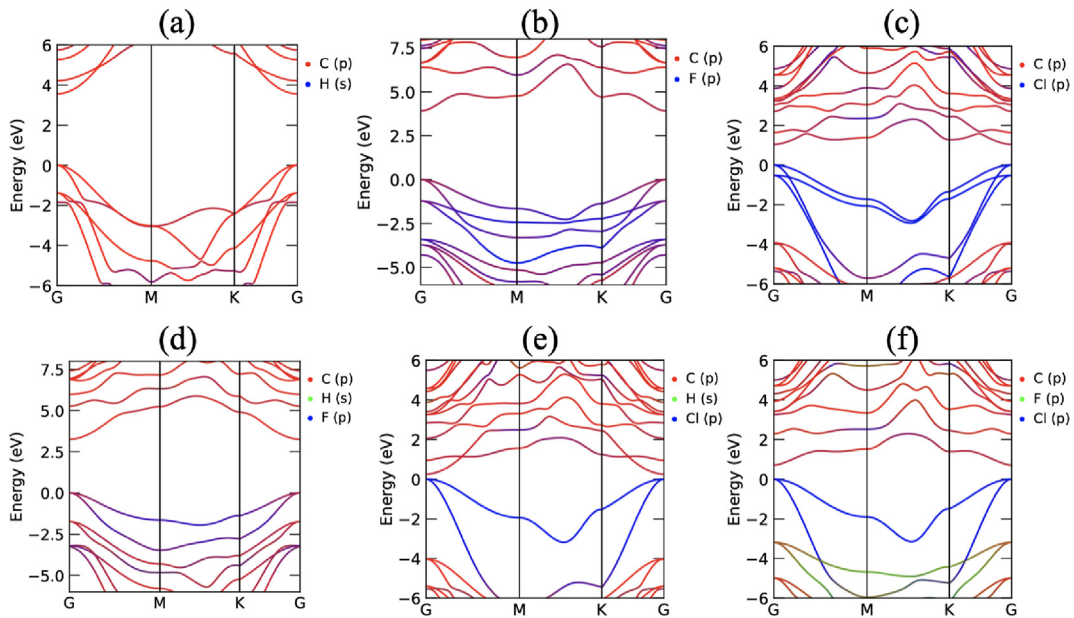


**Fig. 4.** Decomposed electronic band structures of freestanding Janus and non-Janus diamanes of (a)  $\text{C}_2\text{H}$ , (b)  $\text{C}_2\text{F}$ , (c)  $\text{C}_2\text{Cl}$ , (d)  $\text{C}_4\text{HF}$ , (e)  $\text{C}_4\text{HCl}$  and (f)  $\text{C}_4\text{FCl}$  monolayers.

materials are 3.85, 5.64, 2.32, 4.16, 0.73 and 1.91 eV for  $\text{C}_2\text{H}$ ,  $\text{C}_2\text{F}$ ,  $\text{C}_2\text{Cl}$ ,  $\text{C}_2\text{HF}$ ,  $\text{C}_2\text{HCl}$  and  $\text{C}_2\text{FCl}$  monolayers, respectively. It is clearly seen that the non-Janus monolayer displayed a higher band gap as compared to Janus monolayer except  $\text{C}_2\text{HF}$  because F containing

non-Janus monolayer have a very high band gap. In addition, the  $\text{C}_2\text{H}$  and  $\text{C}_2\text{F}$  non-Janus monolayers have relatively higher band gaps. When H and F are combined together, the band gap is reduced, but it's higher than  $\text{C}_2\text{H}$  monolayer. The Cl containing

**Table 2**

Calculated electronic band gap (eV) using GGA-PBE and HSE06 functionals and effective mass of electron ( $m_e^*$ ) and hole ( $m_h^*$ ) along G-K direction and charge transfer from carbon atoms towards the H, F and Cl atoms using Bader charge analysis for non-Janus and Janus monolayers.

System	$E_g(\text{GGA - PBE})$	$E_g(\text{HSE06})$	$m_e^*$	$m_h^*$	$\Delta Q_1$	$\Delta Q_2$
C <sub>2</sub> H	3.57	3.85	0.321	0.237	-0.10(H)	-0.10(H)
C <sub>2</sub> F	3.92	5.64	0.179	0.357	-0.23(F)	-0.23(F)
C <sub>2</sub> Cl	1.04	2.32	0.328	0.412	-0.04(Cl)	-0.04(Cl)
C <sub>4</sub> HF	2.53	3.26	0.33	0.34	-0.10(H)	-0.55(F)
C <sub>4</sub> HCl	0.25	0.73	0.32	0.426	-0.17(H)	-0.03(Cl)
C <sub>4</sub> FCl	0.71	1.91	0.248	0.43	-0.48(F)	-0.041(Cl)

Janus monolayer significantly suppressed the band gap because the Cl containing non-Janus monolayer has relatively less band gap as compared to others. Table 2 represents the effective mass of charge carriers for electrons and holes. The calculated effective masses of the holes ( $m_h^*/m_0$ ) and electrons ( $m_e^*/m_0$ ) for the VBM and CBM of the Janus monolayers are as follows [92],

$$m^* = \hbar^2 \left[ \frac{\partial^2 E(k)}{\partial k^2} \right]^{-1}, \quad (4)$$

where  $\hbar$  is the Plank constant,  $k$  is the wave vector and  $E(k)$  represent the respective energy dispersion in VBM and CBM. The effective mass of electrons is relatively smaller than that of holes, except for C<sub>2</sub>H. Due to the presence of a small charge carrier effective mass Janus and non-Janus diamanes monolayers are very useful in the fields of optoelectronics and high-performance nanoelectronics devices.

Further, to understand the contribution of electronic states in the valence band maximum (VBM) and conduction band minimum (CBM), we have calculated the projected density of states (PDOS). Fig. 5 shows the PDOS of the Janus and non-Janus diamanes

monolayers. In the case of C<sub>2</sub>H, the C-p states are contributed in both VBM and CBM near to the Fermi level and very little contribution comes from H-s states (see Fig. 5a). The H-s states it appears below -2 eV in the VBM. It means that the electronic band gap is mainly originated by the C atom in the C<sub>2</sub>H monolayer, which is reflected in the orbital contributed electronic band structure (Fig. 4a). Fig. 5b shows the PDOS of C<sub>2</sub>F monolayer, the C-p states, and F-p states are contributed in the VBM near to the Fermi level while CBM is mainly made by C-p states. It is clear from Fig. 5b, the C-p states are more dominant as compared to F-p states. It means that C-p states are strongly hybridized with F-p states. While in the case of C<sub>2</sub>Cl monolayer, the top of the VBM is made by Cl-p states, and the bottom of the CBM is mainly made by C-p states. It means that the electronic band gap is mainly originated by Cl-p states and C-p states. Further, when a single H atom is replaced by an F atom i.e. Janus C<sub>4</sub>HF monolayer, then p-states of C and F atoms are more dominant near the Fermi level. It means that the electronic states of both C and F atoms are strongly hybridized. Also, the bottom of the CBM is made by C-p states, and a small contribution comes from F-p states. In the case of C<sub>4</sub>HCl and C<sub>4</sub>FCl, the top of the VBM is dominated by Cl-p states while the bottom of the CBM is formed by C-p states, and a small contribution comes from other atoms which are clearly reflected in the decomposed electronic band structures (see Fig. 4).

### 3.4. Optical properties

The potential and efficiency of sunlight harvesting represent another exciting aspect for characterizing and evaluating the performance of photo-catalytic devices. In this regard, the optical properties of Janus and non-Janus diamanes C<sub>2</sub>H, C<sub>2</sub>F, C<sub>2</sub>Cl, C<sub>4</sub>HF, C<sub>4</sub>HCl and C<sub>4</sub>FCl monolayers are explored by means of the complex dielectric function  $\epsilon(\omega)$ , which is given through the following relation:

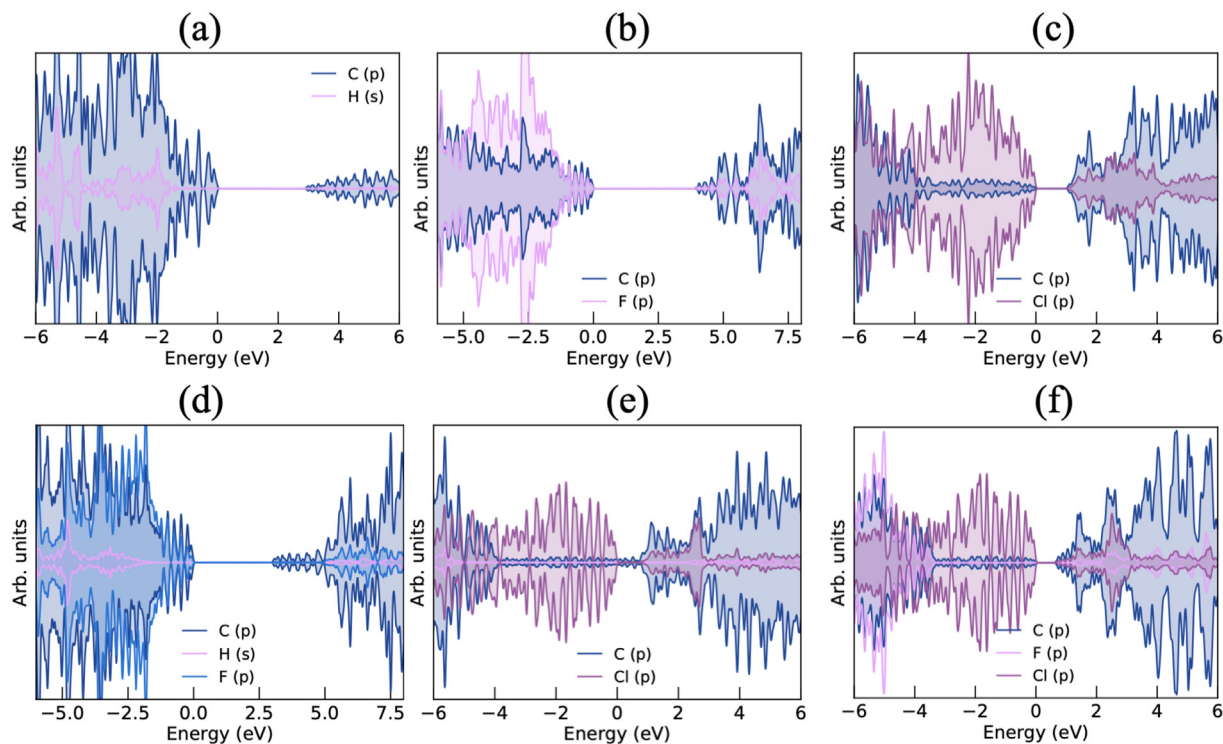


Fig. 5. The calculated projected density of states of freestanding Janus and non-Janus diamanes of (a) C<sub>2</sub>H, (b) C<sub>2</sub>F, (c) C<sub>2</sub>Cl, (d) C<sub>4</sub>HF, (e) C<sub>4</sub>HCl and (d) C<sub>4</sub>FCl monolayers.

$$\epsilon(\omega) = \epsilon_1(\omega) + i\epsilon_2(\omega) \quad (5)$$

where  $\epsilon_1(\omega)$  and  $\epsilon_2(\omega)$  represents the real/imaginary part of  $\epsilon(\omega)$ , respectively. The real/imaginary part of the complex dielectric function for Janus and non-Janus diamanes materials are illustrated in Fig. 6a,b. First, it can be clearly noticed from the real part of the dielectric function that the static dielectric constants of  $C_2H$ ,  $C_2F$ ,  $C_2Cl$ ,  $C_4HF$ ,  $C_4HCl$  and  $C_4FCl$  monolayers are respectively 2.17, 3.33, 2.16, 4.82, and 2.95 with a positive trend over the whole considered energy-level ranging between 0 and 5 eV, confirming the semiconducting behavior of the 2D Janus and non-Janus diamanes monolayers. Moreover, once the peak values are reached, the  $\epsilon_1(\omega)$  of the investigated Janus and non-Janus monolayers decrease with some slight fluctuations. Furthermore, it can be clearly noticed from the imaginary part of  $\epsilon(\omega)$  of the six considered materials the presence of at least one peak with a great value in the case of  $C_2F$  at 0.3 eV, resulting from the transitions between the occupied VB to unoccupied CB.

On the other hand, with regard to the optical features of the concerned materials, it is worth mentioning that they can be more

precisely characterized by the complex refractive index given by the following formula:

$$\tilde{n}(\omega) = n(\omega) + ik(\omega) \quad (6)$$

With the  $n(\omega)/k(\omega)$  refers to the real/imaginary terms in the complex refractive index  $\tilde{n}(\omega)$ . From the Fig. 6c,d, it can be observed that the complex refractive index slightly vary across the entire considered energy range of 0–6 eV with a static refractive index ( $\tilde{n}(0)$ ) equal approximately to 1.45 in the case of  $C_2H$ ,  $C_4HF$ ,  $C_4HCl$  and about 1.73, 1.86, 2.46 in the case of  $C_2FCl$ ,  $C_2Cl$ , and  $C_2F$ , respectively. Additionally, the extinction coefficient shows a great peak in the visible zone for the 2D non-Janus  $C_4HF$ ,  $C_4HCl$ , and  $C_4FCl$  monolayers, while for the 2D Janus  $C_2H$ ,  $C_2F$ , and  $C_2Cl$  the peak appears in the ultraviolet zone, suggesting that the photons-absorption are higher around these energies-levels.

In addition, the optical absorption coefficient spectrum, which defines the decay of light migrating over the distance-unit in an absorbing material with the electron energy-loss function, was calculated within HSE06 functional according to the following equations and plotted in Fig. 6e,f:

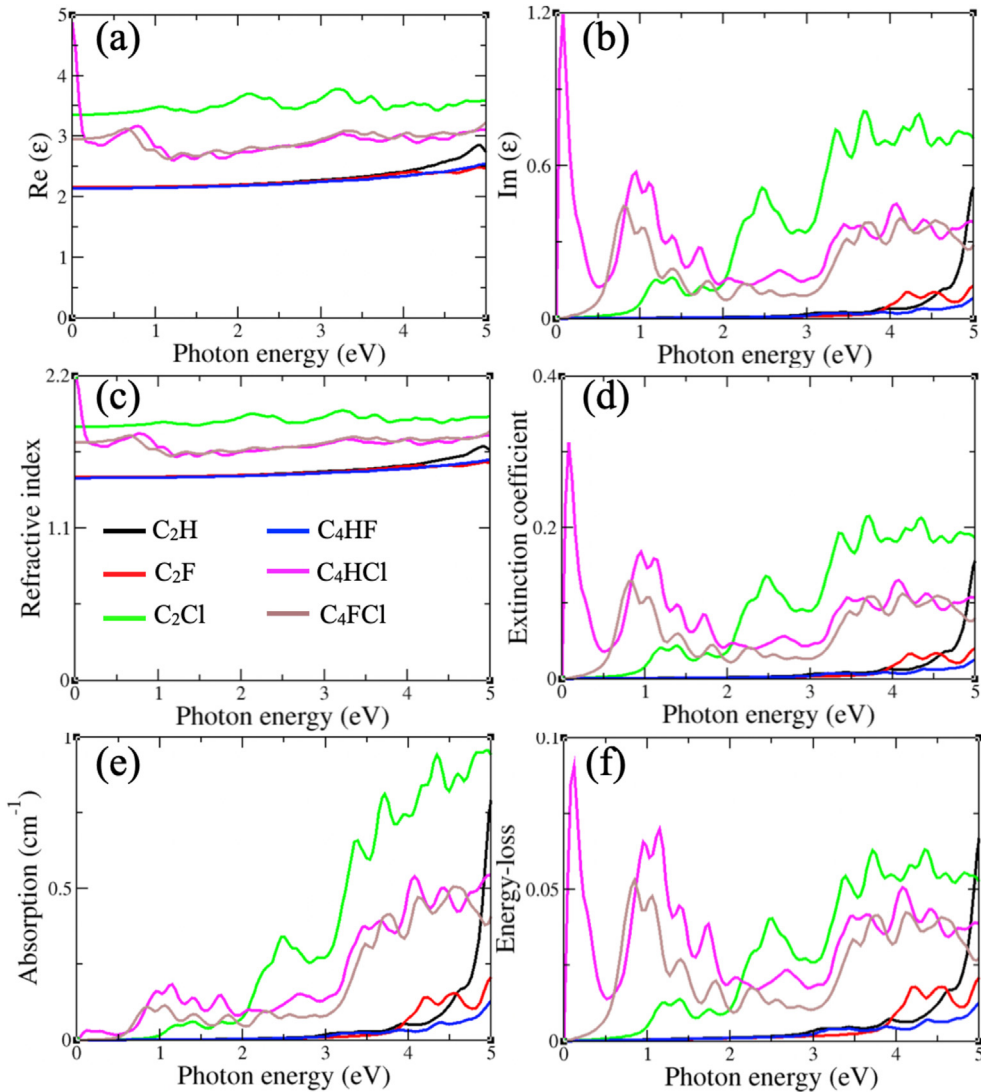


**Fig. 6.** Optical properties as a function of photon energy of freestanding Janus and non-Janus diamanes monolayers, (a) real part of dielectric function, (b) imaginary part of dielectric function, (c) refractive index, (d) extinction coefficient, (e) absorption coefficient ( $\times 10^5$ ) and (d) electron energy loss function.

$$\alpha(\omega) = \sqrt{2\omega} \left[ \sqrt{\varepsilon_1(\omega)^2 + \varepsilon_2(\omega)^2} + \varepsilon_2(\omega) \right]^{1/2} \quad (7)$$

$$L(\omega) = \frac{\varepsilon_2(\omega)^2}{\varepsilon_1(\omega)^2 + \varepsilon_2(\omega)^2} \quad (8)$$

It can be obviously noticed that the absorption coefficient spectrum  $\alpha(\omega)$  presents various peaks within the considered energy level of 0–5 eV. The computed absorption coefficient is equal to zero when the photon-energy is lower than approximately 2.9 eV for  $C_2H$ ,  $C_2F$ , and  $C_4HF$ , monolayers, while is about 0.9 and 0.5 eV for  $C_2Cl$  and  $C_4FCl$  monolayers, respectively. It can be further remarked that H-, F- and HF-diamane monolayers, present no absorption coefficient spectrum in the visible-light zone, but a good absorption coefficient spectrum with the highest peaks obtained relatively around  $10^5 \text{ cm}^{-1}$  in the ultra-violet zone (4.13–6.20 eV), which is in good agreement with their wide electronic band gaps ( $>3.85 \text{ eV}$ ) compared to Cl-based diamane monolayers. It can also be noticed that Cl-based diamane systems exhibit a peak in the energy range of the visible-light region (2–3.2 eV) in the case of  $C_2Cl$  monolayer and a small peak in the mid-infrared light region for the  $C_4HCl$  and  $C_4FCl$  monolayers. These findings show that Cl-based diamane monolayers may be interesting candidates for visible-light optoelectronic applications and many other areas, from environmental gas monitoring to the detection of pharmaceuticals.

### 3.5. Photocatalytic activity of Janus and non-Janus diamanes monolayers

Based on the optical absorption coefficient, it is anticipated that 2D Janus and non-Janus diamanes monolayer photocatalysts provide outstanding photocatalytic activity performance. For this purpose, detailed and accurate comprehension of the valence and conduction band edge positions at pH = 0 as a function of the standard hydrogen electrode (SHE) of the six considered monolayers is crucial. Within the scope of this study, given that the PBE-GGA exchange-correlation functional commonly underestimates the electronic band gap of materials, thereby adversely affecting the main finding of the valence/conduction band-edge positions. The HSE06 exchange-correlation functional is exclusively taken into account during the valence and conduction band-edge positions of 2D Janus and non-Janus diamanes monolayers within the following equations:

$$E_{VBM} = (\chi - E_e + E_g^{HSE-06})/2 \quad (9)$$

$$E_{CBM} = E_{VBM} - E_g^{HSE-06} \quad (10)$$

The  $\chi$  represents the electronegativity of the 2D Janus and non-Janus diamanes monolayers, and the  $E_e$  represents the energy of a free electron, which really is nearly 4.5 eV. Fig. 7 illustrate the schematic diagram of the conduction and valence band-edge positions calculated by means of the HSE06 exchange-correlation for the considered monolayers functional simultaneously with the reduction ( $H^+/H_2$ ) and oxidation ( $O_2/H_2O$ ) potential for the water splitting. It can be clearly seen that a favorable valence and conduction band-edge position for the 2D Janus and non-Janus diamanes monolayers are obtained, excluding both 2D non-Janus ( $C_4HCl$  and  $C_4FCl$ ) monolayers showing an  $E_{VBM}$  inferior to the reduction-potential ( $H^+/H_2$ ) marked by the black dashed line. However, the locations of the VB- and CB-edge for the 2D Janus ( $C_2H$ ,  $C_2F$ , and  $C_2Cl$ ) as well as the non-Janus ( $C_4HF$ ) monolayers

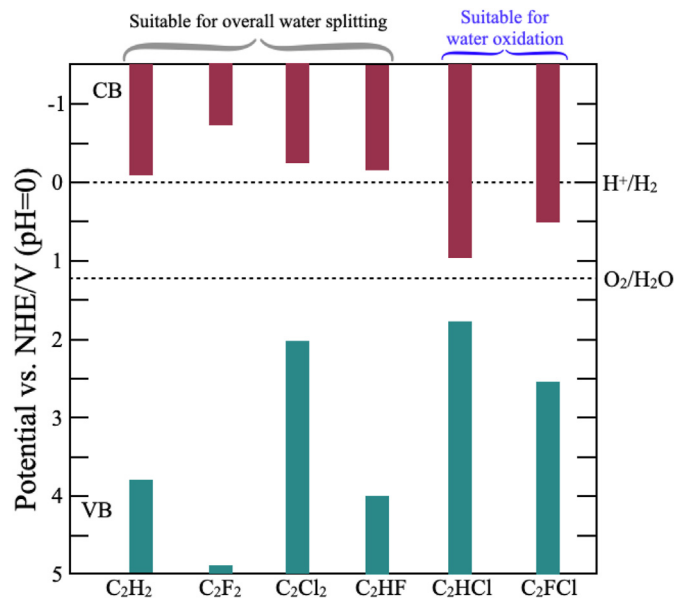


**Fig. 7.** Computed valence and conduction band-edge position of 2D Janus diamanes of  $C_2H$ ,  $C_2F$ , and  $C_2Cl$  and 2D non-Janus diamanes  $C_4HF$ ,  $C_4HCl$ , and  $C_4FCl$  monolayers.

straddling the HER and OER redox-levels strongly indicate the fact that they yield suitable and thermodynamically appropriate conditions for the water-splitting mechanisms [93].

Furthermore, the Janus monolayers displayed non-centrosymmetric structure therefore it has a very high electrostatic potential difference of 1.88, 1.70 and 1.94 eV for  $C_4HF$ ,  $C_4HCl$  and  $C_4FCl$ , respectively between X ( $X = H/F$ ) and Y ( $Y=F,Cl$ ) sites which generates an internal electric field in the Janus monolayers. Due to the presence of different values of electrostatic potential on X ( $X = H/F$ ) and Y ( $Y=F,Cl$ ) sites, Janus monolayers shows spontaneous internal electron transfer from H to F side in  $C_4HF$ , Cl to H side in  $C_4HCl$  and Cl to F side in  $C_4FCl$  (see Table 2). As a results, these differences in electrostatic potential shows redistribution of charge in the Janus monolayers as compared to the symmetric 2D monolayers. The charge transfer always occurs from lower potential to higher potential [94]. The significant amount of electron transfer as well as an internal electric field generated from one side to other side may explain the large value of the piezoelectric coefficient of Janus monolayers which is discussed in below section. Also, it will effectively enhance the generations of photogenerated electrons ( $e^-$ ) and holes ( $h^+$ ) pairs therefore it will be beneficial for photocatalytic activity.

### 3.6. Piezoelectric properties

Moreover, we have systematically investigated the piezoelectric properties of 2D non-Janus diamanes monolayers. For piezoelectric properties, we initially calculated the elastic stiffness coefficient. Here, the relaxed-ion elastic stiffness coefficient (i.e. the atomic positions are fully relaxed under each strain) is adopted. The range of applied strain varies from –0.005 to 0.005 with an interval of 0.001. Table S1 in SM displays the in-plane elastic stiffness coefficient values for 2D non-Janus diamanes monolayers. The elastic stiffness coefficient  $C_{11}$  is found to be 515, 452.91 and 484.44 N/m whereas  $C_{11}$  are relatively lower at 49.64, 48.97 and 58.99 N/m, for  $C_4HF$ ,  $C_4HCl$  and  $C_4FCl$ , respectively. The elastic stiffness coefficients are significantly higher than the previously reported literature's for 2D monolayer materials such as  $MoS_2$  ( $C_{11} = 138.5$  and  $C_{12} = 31.7 \text{ N/m}$ ) [95],  $PtS_2$  ( $C_{11} = 107.5$  and  $C_{12} = 31.5 \text{ N/m}$ ) [96],  $GaS$  ( $C_{11} = 108$

and  $C_{12} = 32 \text{ N/m}$  [97], and Janus structures MoSSe ( $C_{11} = 126.8$  and  $C_{12} = 27.4 \text{ N/m}$ ) [98], PtSSe ( $C_{11} = 101.6$  and  $C_{12} = 30.3 \text{ N/m}$ ) [96], etc., exhibit that 2D non-Janus diamanes monolayers have a less flexibility. Such type of high values of  $C_{11}$  in 2D non-Janus diamanes monolayers may be ascribed due to the inherent strong ionic bond between the C and X (X = F, Cl) atoms [99].

Now, we will discuss the piezoelectric properties. The presence of symmetry structures of 2D Janus diamanes of  $\text{C}_2\text{H}$ ,  $\text{C}_2\text{F}$  monolayers, doesn't show piezoelectricity. Whereas the presence of asymmetry structures in non-Janus diamanes monolayers has a piezoelectric effect. It is well known that piezoelectricity is the result of electromechanical interaction, which is generally defined by piezoelectric coefficients, and detailed equations are presented in Ref. [99]. It was seen that the in-plane and out-of-plane piezoelectric coefficient  $e_{11}$  and  $e_{31}$  have non-zero terms. Initially, we have investigated the non-zero term  $e_{11}$  and  $e_{31}$  using density functional perturbation theory (DFPT) after that  $d_{11}$  and  $d_{31}$  has been calculated by following relations;

$$e_{11} = d_{11}(C_{11} - C_{12}), \quad (11)$$

$$e_{31} = d_{31}(C_{11} + C_{12}) \quad (12)$$

The calculated relaxed-ion piezoelectric coefficients of 2D non-Janus diamanes  $\text{C}_4\text{HF}$ ,  $\text{C}_4\text{HCl}$ , and  $\text{C}_4\text{FCl}$  monolayers ( $e_{11} = 12.39 \times 10^{-10} \text{ C/m}$ ,  $d_{11} = 2.20 \text{ pm/V}$ ,  $e_{11} = 9.46 \times 10^{-10} \text{ C/m}$ ,  $d_{11} = 1.86 \text{ pm/V}$  and  $e_{11} = 12.35 \times 10^{-10} \text{ C/m}$ ,  $d_{11} = 2.27 \text{ pm/V}$ ), respectively. The investigated values of piezoelectric coefficients are of the same order as the previously reported materials [100], such as BN monolayer ( $e_{11} = 1.38 \times 10^{-10} \text{ C/m}$ ,  $d_{11} = 0.60 \text{ pm/V}$ ) [95], GaS monolayer  $e_{11} = 1.34 \times 10^{-10} \text{ C/m}$ ,  $d_{11} = 2.06 \text{ pm/V}$ ) [97], GaSe monolayer  $e_{11} = 1.47 \times 10^{-10} \text{ C/m}$ ,  $d_{11} = 2.30 \text{ pm/V}$ ) [97], InSe monolayer  $e_{11} = 0.57 \times 10^{-10} \text{ C/m}$ ,  $d_{11} = 1.46 \text{ pm/V}$ ) [97] but slightly lower than the MoS<sub>2</sub> monolayer ( $e_{11} = 3.64 \times 10^{-10} \text{ C/m}$ ,  $d_{11} = 3.73 \text{ pm/V}$ ) [95]. The out-of-plane piezoelectric coefficient  $e_{31}$  and  $d_{31}$  are found to be in the range of  $0.004\text{--}0.68 \times 10^{-10} \text{ C/m}$  and  $0.001\text{--}0.17 \text{ pm/V}$ , respectively which is very lower than in-plane. It means that, the in-plane piezoelectric coefficient are dominant in 2D non-Janus diamanes monolayer similar to other 2D monolayer materials. The above finding results of piezoelectric coefficient in the 2D non-Janus diamanes monolayers could be very useful in the fields of piezoelectric applications.

### 3.7. Thermoelectric properties

At last, we have systematically investigated the thermoelectric parameters such as Seebeck coefficient (S), electrical conductivity ( $\sigma$ ), electronic thermal conductivity ( $\kappa_e$ ) using BoltzTraP code and

lattice thermal conductivity ( $\kappa_l$ ) by ShengBTE code. After that, with the combinations of these thermoelectric parameters, we have calculated the thermoelectric figure of merit (ZT) and thermoelectric conversion efficiency ( $\eta$ ). The detailed descriptions of the Seebeck coefficient, electrical conductivity, electronic thermal conductivity, and lattice thermal conductivity with p-type and n-type (see Fig. S6 and Fig. S7) have been discussed in Supporting Information.

Here, we will discuss the thermoelectric figure of merit (ZT) of 2D Janus diamanes of  $\text{C}_2\text{H}$ ,  $\text{C}_2\text{F}$ , and  $\text{C}_2\text{Cl}$  and 2D non-Janus diamanes  $\text{C}_4\text{HF}$ ,  $\text{C}_4\text{HCl}$ , and  $\text{C}_4\text{FCl}$  monolayers. The thermoelectric ZT values for the p-type and n-type are presented in Fig. 8a,b, respectively. For efficient thermoelectric materials i.e. higher ZT values, the values of S and  $\sigma$  should be higher and  $\kappa$  should be lower values. It was seen that the p-type monolayer  $\text{C}_2\text{H}$  displayed higher ZT values at 300 K overall in the studied temperature region as compared to n-type due to the relatively higher electrical conductivity. Also,  $\text{C}_2\text{F}$  monolayer has higher ZT values at 300 K as compared to other Janus diamanes and non-Janus diamanes monolayers. Moreover, the ZT values of Janus diamanes and non-Janus diamanes monolayers are obviously higher than those of previously reported work such as 0.08 for a single layer of graphene [101], and 0.12 for  $\beta$ -, 0.03 for  $\alpha$ -, 0.05 for (6,6,12)-, and 0.17 for  $\gamma$ -graphyne [102,103],  $\approx 0.38$  in CP [104],  $\approx 0.75$  in arsenene [105],  $\approx 0.78$  in antimonene [105]. The maximum ZT values are found to be 0.93 at 300 K and 0.1 at 1000 K and the average values of ZT is 0.515 in  $\text{C}_2\text{H}$  monolayer for p-type whereas 0.8 at 300 K and 0.24 at 1000 K in  $\text{C}_2\text{F}$  monolayer for n-type in which the average ZT value is 0.52.

Further, we have calculated the thermoelectric performance of thermoelectric materials in which the thermoelectric conversion efficiency is the main parameter for the performance of devices. Therefore, we have investigated the thermoelectric conversion efficiency  $\eta_{max}$  based on average ZT values and it is calculated by the following relation:

$$\eta_{max} = \frac{T_h - T_c}{T_h} \frac{\sqrt{1 + (ZT)_{avg}} - 1}{\sqrt{1 + (ZT)_{avg} + \frac{T_c}{T_h}}} \quad (13)$$

Here,  $T_c$  and  $T_h$  are the considered temperatures of the cold side and hot side, respectively. In this work, we have taken the temperatures of 300 K and 1000 K for the cold side and hot side to calculate the thermoelectric conversion efficiency. The calculated conversion efficiency are 10.52% and 10.63% for  $\text{C}_2\text{H}$  and  $\text{C}_2\text{F}$  monolayer, respectively, which is higher than the previously investigated thermoelectric devices such as Bi<sub>2</sub>Te<sub>3</sub> devices ( $\eta_{max} = \sim 6.6$ ,  $\Delta T = 275 \text{ K}$ ) [106] and MgAgSb ( $\eta_{max} = \sim 10$ ,

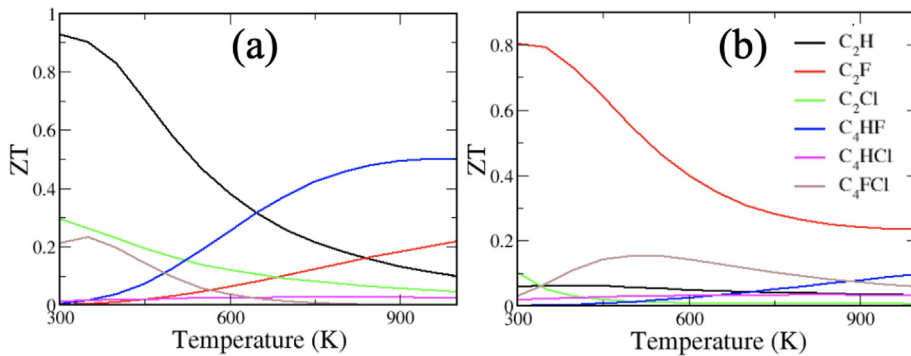


**Fig. 8.** Thermoelectric figure of merit (ZT) as a function of temperature of 2D Janus diamanes of  $\text{C}_2\text{H}$ ,  $\text{C}_2\text{F}$ , and  $\text{C}_2\text{Cl}$  and 2D non-Janus diamanes  $\text{C}_4\text{HF}$ ,  $\text{C}_4\text{HCl}$ , and  $\text{C}_4\text{FCl}$  monolayers.

$\Delta T = 275 \text{ K}$  [107]. Based on the above observations, the 2D Janus diamanes, and non-Janus diamanes monolayers are very useful in potential applications in various fields.

#### 4. Conclusions

We have systematically investigated the structural, mechanical, electronic, optical, photocatalytic, piezoelectric, and thermoelectric properties of non-Janus and Janus diamanes monolayers using first-principles calculations based on density functional theory. From the cohesive energy, phonon band structures, and mechanical properties investigations, it has been confirmed that the non-Janus and Janus diamanes monolayers displayed structural stability. From the electronic properties, these considered non-Janus and Janus diamanes monolayers have semiconducting behaviors with a direct band gap at the G point. The calculated band gaps are 3.85, 5.64, 2.32, 4.16, 0.73 and 1.91 eV for  $C_2H$ ,  $C_2F$ ,  $C_2Cl$ ,  $C_2HF$ ,  $C_2HCl$  and  $C_2FCl$  monolayers, respectively. The mechanical properties result, such as Poisson's ratio, have negative values, which means that such types of materials show good auxetic properties. In our case, the negative Poisson's ratio is found higher in hydrogen-containing diamanes monolayers than in most of the 2D monolayered materials. Also, the mechanical properties such as Poisson's ratio and Young's modulus displayed anisotropic behaviors. The investigated optical properties displayed refractive index values near to 1.5 therefore,  $C_2H$ ,  $C_2F$ ,  $C_2Cl$ ,  $C_2HF$  monolayers will be fully transparent materials. Additionally, the high absorption spectra in the visible and ultraviolet regions displayed better candidates for optoelectronic devices and photocatalytic applications. Apart from this, its VBM and CBM exhibit straddle the water redox potentials, so it will be very beneficial for overall water splitting. Moreover, the higher values of the in-plane piezoelectric coefficient show that the non-Janus and Janus diamanes monolayers will be good candidates for piezoelectric applications. From the thermoelectric properties, the relatively higher values of the thermoelectric figure of merit as compared to pristine graphene displayed high-performance thermoelectric materials. The non-Janus diamanes monolayers  $C_2H$  and  $C_2F$  have great thermoelectric efficiency, 10.52 and 10.63%, respectively. The discussed results show the non-Janus and Janus diamanes monolayers will be very useful in various applications for energy harvesting devices.

#### Data availability

The raw/processed data required to reproduce these findings cannot be shared at this time as the data also forms part of an ongoing study.

#### Author statement

**Deobrat Singh:** Investigation, Methodology, Visualization, Formal analysis, Writing – original draft. **Nabil Khossossi:** Conceptualization, Formal analysis, Investigation, Methodology, Writing – review & editing, Validation. **Wei Luo:** Writing – review & editing, Validation. **Abdelmajid Ainane:** Writing – review & editing, Validation. **Rajeev Ahuja:** Funding acquisition, Project administration, Resources, Software, Supervision, Writing – review & editing, Validation.

#### Declaration of competing interest

The authors declare that they have no known competing financial interests or personal relationships that could have appeared to influence the work reported in this paper.

#### Acknowledgements

D.S., N.K., W.L., and R.A. gratefully acknowledge computational resources from the Swedish National Infrastructure for Computing SNIC (2021/1-42) and HPC2N. D.S., N.K., W.L., and R.A. thanks the Swedish Research Council (VR-2016-06014 & VR-2020-04410) and J. Gust. Richert stiftelse, Sweden (2021-00665) for financial support. A.A. acknowledge support from the PPR2 Project (MESRSF-CNRST).

#### Appendix A. Supplementary data

Supplementary data to this article can be found online at <https://doi.org/10.1016/j.mtadv.2022.100225>.

#### References

- [1] K.S. Novoselov, A.K. Geim, S.V. Morozov, D.-e. Jiang, Y. Zhang, S.V. Dubonos, I.V. Grigorieva, A.A. Firsov, Electric field effect in atomically thin carbon films, *Science* 306 (5696) (2004) 666–669.
- [2] A.K. Geim, K.S. Novoselov, The rise of graphene, in: *Nanoscience and Technology: a Collection of Reviews from Nature Journals*, World Scientific, 2010, pp. 11–19.
- [3] J.D. Caldwell, I. Aharonovich, G. Cassabois, J.H. Edgar, B. Gil, D. Basov, Photonics with hexagonal boron nitride, *Nat. Rev. Mater.* 4 (8) (2019) 552–567.
- [4] B. Zeng, M. Li, X. Zhang, Y. Yi, L. Fu, M. Long, First-principles prediction of the electronic structure and carrier mobility in hexagonal boron phosphide sheet and nanoribbons, *J. Phys. Chem. C* 120 (43) (2016) 25037–25042.
- [5] N. Khossossi, Y. Benhouria, S.R. Naqvi, P.K. Panda, I. Essaoudi, A. Ainane, R. Ahuja, Hydrogen storage characteristics of Li and Na decorated 2d boron phosphide, *Sustain. Energy Fuels* 4 (9) (2020) 4538–4546.
- [6] N. Khossossi, P.K. Panda, D. Singh, V. Shukla, Y.K. Mishra, I. Essaoudi, A. Ainane, R. Ahuja, Rational design of 2d h-bas monolayer as advanced sulfur host for high energy density Li-S batteries, *ACS Appl. Energy Mater.* 3 (8) (2020) 7306–7317.
- [7] N. Khossossi, A. Banerjee, I. Essaoudi, A. Ainane, P. Jena, R. Ahuja, Thermodynamics and kinetics of 2d g-gec monolayer as an anode materials for Li/Na-ion batteries, *J. Power Sources* 485 (2021) 229318.
- [8] S. Manzeli, D. Ovchinnikov, D. Pasquier, O.V. Yazyev, A. Kis, 2d transition metal dichalcogenides, *Nat. Rev. Mater.* 2 (8) (2017) 1–15.
- [9] R. Ahmed, N. Jena, A. Rawat, M.K. Mohanta, Dimple, A. De Sarkar, Ultra-high out-of-plane piezoelectricity meets giant Rashba effect in 2d Janus monolayers and bilayers of group IV transition-metal trichalcogenides, *J. Phys. Chem. C* 124 (39) (2020) 21250–21260.
- [10] W. Choi, N. Choudhary, G.H. Han, J. Park, D. Akinwande, Y.H. Lee, Recent development of two-dimensional transition metal dichalcogenides and their applications, *Mater. Today* 20 (3) (2017) 116–130.
- [11] M. Yagmurcukardes, Y. Qin, S. Ozen, M. Sayyad, F.M. Peeters, S. Tongay, H. Sahin, Quantum properties and applications of 2d Janus crystals and their superlattices, *Appl. Phys. Rev.* 7 (1) (2020), 011311.
- [12] M.J. Varjovi, M. Yagmurcukardes, F. Peeters, E. Durgun, Janus two-dimensional transition metal dichalcogenide oxides: first-principles investigation of  $W_xO$  monolayers with  $x = s, se,$  and  $te$ , *Phys. Rev. B* 103 (19) (2021) 195438.
- [13] M. Demirtas, M.J. Varjovi, M. Cicek, E. Durgun, Tuning structural and electronic properties of two-dimensional aluminum monochalcogenides: prediction of Janus  $Al_{2xx'}(x/x': O, s, se, te)$  monolayers, *Phys. Rev. Mater.* 4 (11) (2020) 114003.
- [14] Z. Haman, N. Khossossi, M. Kibbou, I. Bouziani, D. Singh, I. Essaoudi, A. Ainane, R. Ahuja, Computational identification of efficient 2d aluminium chalcogenides monolayers for optoelectronics and photocatalysts applications, *Appl. Surf. Sci.* 556 (2021) 149561.
- [15] P. Nandi, A. Rawat, R. Ahmed, N. Jena, A. De Sarkar, Group-IV (a) Janus dichalcogenide monolayers and their interfaces straddle gigantic shear and in-plane piezoelectricity, *Nanoscale* 13 (10) (2021) 5460–5478.
- [16] L. Li, C. Bacaksiz, M. Nakhaee, R. Pentcheva, F. Peeters, M. Yagmurcukardes, Single-layer Janus black arsenic-phosphorus (b-asp): optical dichroism, anisotropic vibrational, thermal, and elastic properties, *Phys. Rev. B* 101 (13) (2020) 134102.
- [17] M.-Y. Liu, L. Gong, Y. He, C. Cao, Tuning Rashba effect, band inversion, and spin-charge conversion of Janus  $s n 2 y$  monolayers via an external field, *Phys. Rev. B* 103 (7) (2021), 075421.
- [18] W.-L. Tao, J.-Q. Lan, C.-E. Hu, Y. Cheng, J. Zhu, H.-Y. Geng, Thermoelectric properties of Janus  $mxy$  ( $m = pd, pt; x, y = s, se, te$ ) transition-metal dichalcogenide monolayers from first principles, *J. Appl. Phys.* 127 (3) (2020), 035101.
- [19] A. Kandemir, H. Sahin, Janus single layers of  $s se$ : a first-principles study, *Phys. Rev. B* 97 (15) (2018) 155410.
- [20] Y. Wang, W. Wei, H. Wang, N. Mao, F. Li, B. Huang, Y. Dai, Janus  $tixy$  monolayers with tunable Berry curvature, *J. Phys. Chem. Lett.* 10 (23) (2019)

- 7426–7432.
- [21] M. Naguib, V.N. Mochalin, M.W. Barsoum, Y. Gogotsi, 25th anniversary article: mxenes: a new family of two-dimensional materials, *Adv. Mater.* 26 (7) (2014) 992–1005.
- [22] Z. Fu, N. Wang, D. Legut, C. Si, Q. Zhang, S. Du, T.C. Germann, J.S. Francisco, R. Zhang, Rational design of flexible two-dimensional mxenes with multiple functionalities, *Chem. Rev.* 119 (23) (2019) 11980–12031.
- [23] Z. Dai, L. Liu, Z. Zhang, Strain engineering of 2d materials: issues and opportunities at the interface, *Adv. Mater.* 31 (45) (2019) 1805417.
- [24] A.K. Singh, K. Mathew, H.L. Zhuang, R.G. Hennig, Computational screening of 2d materials for photocatalysis, *J. Phys. Chem. Lett.* 6 (6) (2015) 1087–1098.
- [25] B. Liu, A. Abbas, C. Zhou, Two-dimensional semiconductors: from materials preparation to electronic applications, *Adv. Electr. Mater.* 3 (7) (2017) 1700045.
- [26] J. Cheng, C. Wang, X. Zou, L. Liao, Recent advances in optoelectronic devices based on 2d materials and their heterostructures, *Adv. Opt. Mater.* 7 (1) (2019) 1800441.
- [27] A. Thomas, A. Fischer, F. Goettmann, M. Antonietti, J.-O. Müller, R. Schlögl, J.M. Carlsson, Graphitic carbon nitride materials: variation of structure and morphology and their use as metal-free catalysts, *J. Mater. Chem.* 18 (41) (2008) 4893–4908.
- [28] S. Lyth, Y. Nabae, N. Islam, S. Kuroki, M. Kakimoto, S. Miyata, Electrochemical oxygen reduction activity of carbon nitride supported on carbon black, *J. Electrochem. Soc.* 158 (2) (2010) B194.
- [29] S.M. Lyth, Y. Nabae, S. Moriya, S. Kuroki, M.-a. Kakimoto, J.-i. Ozaki, S. Miyata, Carbon nitride as a nonprecious catalyst for electrochemical oxygen reduction, *J. Phys. Chem. C* 113 (47) (2009) 20148–20151.
- [30] Z. Meng, Y. Xie, T. Cai, Z. Sun, K. Jiang, W.-Q. Han, Graphene-like g-c<sub>3</sub>n<sub>4</sub> nanosheets/sulfur as cathode for lithium-sulfur battery, *Electrochim. Acta* 210 (2016) 829–836.
- [31] J. Zhu, P. Xiao, H. Li, S.A. Carabineiro, Graphitic carbon nitride: synthesis, properties, and applications in catalysis, *ACS Appl. Mater. Interfaces* 6 (19) (2014) 16449–16465.
- [32] Y. Huang, B. Chen, J. Duan, F. Yang, T. Wang, Z. Wang, W. Yang, C. Hu, W. Luo, Y. Huang, Graphitic carbon nitride (g-c<sub>3</sub>n<sub>4</sub>): an interface enabler for solid-state lithium metal batteries, *Angew. Chem.* 132 (9) (2020) 3728–3733.
- [33] J. Mahmood, E.K. Lee, M. Jung, D. Shin, I.-Y. Jeon, S.-M. Jung, H.-J. Choi, J.-M. Seo, S.-Y. Bae, S.-D. Sohn, et al., Nitrogenated holey two-dimensional structures, *Nat. Commun.* 6 (1) (2015) 1–7.
- [34] J. Mahmood, E.K. Lee, M. Jung, D. Shin, H.-J. Choi, J.-M. Seo, S.-M. Jung, D. Kim, F. Li, M.S. Lah, et al., Two-dimensional polyaniline (c<sub>3</sub>n) from carbonized organic single crystals in solid state, *Proc. Natl. Acad. Sci. Unit. States Am.* 113 (27) (2016) 7414–7419.
- [35] J. Zeng, Z. Chen, X. Zhao, W. Yu, S. Wu, J. Lu, K.P. Loh, J. Wu, From all-triazine c<sub>3</sub>n<sub>3</sub> framework to nitrogen-doped carbon nanotubes: efficient and durable trifunctional electrocatalysts, *ACS Appl. Nano Mater.* 2 (12) (2019) 7969–7977.
- [36] J. Xu, J. Mahmood, Y. Dou, S. Dou, F. Li, L. Dai, J.-B. Baek, 2d frameworks of c<sub>2</sub>n and c<sub>3</sub>n as new anode materials for lithium-ion batteries, *Adv. Mater.* 29 (34) (2017) 1702007.
- [37] I.Y. Kim, S. Kim, X. Jin, S. Premkumar, G. Chandra, N.-S. Lee, G.P. Mane, S.-J. Hwang, S. Umapathy, A. Vinu, Ordered mesoporous c<sub>3</sub>n<sub>5</sub> with a combined triazole and triazine framework and its graphene hybrids for the oxygen reduction reaction (orr), *Angew. Chem.* 130 (52) (2018) 17381–17386.
- [38] D. Jariwala, A. Srivastava, P.M. Ajayan, Graphene synthesis and band gap opening, *J. Nanosci. Nanotechnol.* 11 (8) (2011) 6621–6641.
- [39] M. Dvorak, W. Oswald, Z. Wu, Bandgap opening by patterning graphene, *Sci. Rep.* 3 (1) (2013) 1–7.
- [40] S.Y. Zhou, G.-H. Gweon, A. Fedorov, d. First, P. N, W. De Heer, D.-H. Lee, F. Guinea, A.C. Neto, A. Lanzara, Substrate-induced bandgap opening in epitaxial graphene, *Nat. Mater.* 6 (10) (2007) 770–775.
- [41] A.G. Kvashnin, L.A. Chernozatonskii, B.I. Yakobson, P.B. Sorokin, Phase diagram of quasi-two-dimensional carbon, from graphene to diamond, *Nano Lett.* 14 (2) (2014) 676–681.
- [42] P.P. Shinde, V. Kumar, Direct band gap opening in graphene by bn doping: ab initio calculations, *Phys. Rev. B* 84 (12) (2011) 125401.
- [43] X. Fan, Z. Shen, A. Liu, J.-L. Kuo, Band gap opening of graphene by doping small boron nitride domains, *Nanoscale* 4 (6) (2012) 2157–2165.
- [44] P. Gava, M. Lazzari, A.M. Saitta, F. Mauri, Ab initio study of gap opening and screening effects in gated bilayer graphene, *Phys. Rev. B* 79 (16) (2009) 165431.
- [45] J.-C. Charlier, X. Gonze, J.-P. Michenaud, First-principles study of graphite monofluoride (cf) n, *Phys. Rev. B* 47 (24) (1993) 16162.
- [46] J.T. Robinson, J.S. Burgess, C.E. Junkermeier, S.C. Badescu, T.L. Reinecke, F.K. Perkins, M.K. Zalalutdinov, J.W. Baldwin, J.C. Culbertson, P.E. Sheehan, et al., Properties of fluorinated graphene films, *Nano Lett.* 10 (8) (2010) 3001–3005.
- [47] Y.-W. Son, M.L. Cohen, S.G. Louie, Energy gaps in graphene nanoribbons, *Phys. Rev. Lett.* 97 (21) (2006) 216803.
- [48] O. Hod, J.E. Peralta, G.E. Scuseria, Edge effects in finite elongated graphene nanoribbons, *Phys. Rev. B* 76 (23) (2007) 233401.
- [49] R. Balog, B. Jørgensen, L. Nilsson, M. Andersen, E. Rienks, M. Bianchi, M. Fanetti, E. Læggsgaard, A. Baraldi, S. Lizzit, et al., Bandgap opening in graphene induced by patterned hydrogen adsorption, *Nat. Mater.* 9 (4) (2010) 315–319.
- [50] T.C. Nguyen, M. Otani, S. Okada, Semiconducting electronic property of graphene adsorbed on (0001) surfaces of sio 2, *Phys. Rev. Lett.* 106 (10) (2011) 106801.
- [51] J.-H. Chen, C. Jang, S. Xiao, M. Ishigami, M.S. Fuhrer, Intrinsic and extrinsic performance limits of graphene devices on sio 2, *Nat. Nanotechnol.* 3 (4) (2008) 206–209.
- [52] P.B. Sorokin, B.I. Yakobson, Two-dimensional diamond–diamane: current state and further prospects, *Nano Lett.* 21 (13) (2021) 5475–5484.
- [53] H. Shu, Strain effects on stability, electronic and optical properties of two-dimensional c 4 x 2 (x= f, cl, br), *J. Mater. Chem. C* 9 (13) (2021) 4505–4513.
- [54] X. Chen, M. Dubois, S. Radescu, A. Rawal, C. Zhao, Liquid-phase exfoliation of f-diamane-like nanosheets, *Carbon* 175 (2021) 124–130.
- [55] F. Piazza, M. Monthoux, P. Puech, I.C. Gerber, K. Gough, Progress on diamane and diamonoid thin film pressureless synthesis, *Chimia* 7 (1) (2021) 9.
- [56] D. Odokhu, D. Shin, R.S. Ruoff, N. Park, Conversion of multilayer graphene into continuous ultrathin sp 3-bonded carbon films on metal surfaces, *Sci. Rep.* 3 (1) (2013) 1–7.
- [57] C. Ke, D. Fan, C. Chen, D. Guo, X. Li, M. Jiang, X. Hu, Chemically Induced Graphene to Diamond Transition: a Dft Study, *arXiv preprint arXiv:* 2101.11930.
- [58] G. Qin, L. Wu, H. Gou, Diamane: design, synthesis, properties, and challenges, *Funct. Diamond* 1 (1) (2021) 83–92.
- [59] D.C. Elias, R.R. Nair, T. Mohiuddin, S. Morozov, P. Blake, M. Halsall, A.C. Ferrari, D. Boukhvalov, M. Katsonelos, A. Geim, et al., Control of graphene's properties by reversible hydrogenation: evidence for graphane, *Science* 323 (5914) (2009) 610–613.
- [60] R.R. Nair, W. Ren, R. Jalil, I. Riaz, V.G. Kravets, L. Britnell, P. Blake, F. Schedin, A.S. Mayorov, S. Yuan, et al., Fluorographene: a two-dimensional counterpart of teflon, *Small* 6 (24) (2010) 2877–2884.
- [61] M. Huang, P.V. Bakharev, Z.-J. Wang, M. Biswal, Z. Yang, S. Jin, B. Wang, H.J. Park, Y. Li, D. Qu, et al., Large-area single-crystal ab-bilayer and ab-trilayer graphene grown on a cu/ni (111) foil, *Nat. Nanotechnol.* 15 (4) (2020) 289–295.
- [62] S. Rajasekaran, F. Abild-Pedersen, H. Ogasawara, A. Nilsson, S. Kaya, Interlayer carbon bond formation induced by hydrogen adsorption in few-layer supported graphene, *Phys. Rev. Lett.* 111 (8) (2013), 085503.
- [63] P.V. Bakharev, M. Huang, M. Saxena, S.W. Lee, S.H. Joo, S.O. Park, J. Dong, D.C. Camacho-Mojica, S. Jin, Y. Kwon, et al., Chemically induced transformation of chemical vapour deposition grown bilayer graphene into fluorinated single-layer diamond, *Nat. Nanotechnol.* 15 (1) (2020) 59–66.
- [64] G. Kresse, J. Furthmüller, Efficient iterative schemes for ab initio total-energy calculations using a plane-wave basis set, *Phys. Rev. B* 54 (16) (1996) 11169.
- [65] J.P. Perdew, K. Burke, M. Ernzerhof, Generalized gradient approximation made simple, *Phys. Rev. Lett.* 77 (18) (1996) 3865.
- [66] J. Heyd, G.E. Scuseria, M. Ernzerhof, Hybrid functionals based on a screened coulomb potential, *J. Chem. Phys.* 118 (18) (2003) 8207–8215.
- [67] H.J. Monkhorst, J.D. Pack, Special points for brillouin-zone integrations, *Phys. Rev. B* 13 (12) (1976) 5188.
- [68] G. Henkelman, A. Arnaldsson, H. Jónsson, A fast and robust algorithm for bader decomposition of charge density, *Comput. Mater. Sci.* 36 (3) (2006) 354–360.
- [69] L. Chaput, A. Togo, I. Tanaka, G. Hug, Phonon-phonon interactions in transition metals, *Phys. Rev. B* 84 (9) (2011), 094302.
- [70] K. Parlinski, Z. Li, Y. Kawazoe, First-principles determination of the soft mode in cubic zro 2, *Phys. Rev. Lett.* 78 (21) (1997) 4063.
- [71] A. Togo, F. Oba, I. Tanaka, First-principles calculations of the ferroelastic transition between rutile-type and cacl 2-type sio 2 at high pressures, *Phys. Rev. B* 78 (13) (2008) 134106.
- [72] M. Parrinello, A. Rahman, Crystal structure and pair potentials: a molecular-dynamics study, *Phys. Rev. Lett.* 45 (14) (1980) 1196.
- [73] L. Kantorovich, N. Rompotis, Generalized Langevin equation for solids. ii. stochastic boundary conditions for nonequilibrium molecular dynamics simulations, *Phys. Rev. B* 78 (9) (2008), 094305.
- [74] W. Li, J. Carrete, N.A. Katcho, N. Mingo, Shengbte: a solver of the Boltzmann transport equation for phonons, *Comput. Phys. Commun.* 185 (6) (2014) 1747–1758.
- [75] G.K. Madsen, D.J. Singh, Boltztrap. a code for calculating band-structure dependent quantities, *Comput. Phys. Commun.* 175 (1) (2006) 67–71.
- [76] M. Raeisi, B. Mortazavi, E.V. Podryabinkin, F. Shojaei, X. Zhuang, A.V. Shapeev, High thermal conductivity in semiconducting janus and non-janus diamanes, *Carbon* 167 (2020) 51–61.
- [77] L. Panchakarla, K. Subrahmanyam, S. Saha, A. Govindaraj, H. Krishnamurthy, U. Waghmare, C. Rao, Synthesis, structure, and properties of boron-and nitrogen-doped graphene, *Adv. Mater.* 21 (46) (2009) 4726–4730.
- [78] K. Raidongia, A. Nag, K. Hembram, U.V. Waghmare, R. Datta, C. Rao, Bcn: a graphene analogue with remarkable adsorptive properties, *Chem. A Eur. J.* 16 (1) (2010) 149–157.
- [79] K. Hussain, U. Younis, I. Muhammad, Y. Qie, Y. Guo, T. Li, H. Xie, Q. Sun, Three-dimensional porous borocarbonitride bc 2 n with negative Poisson's ratio, *J. Mater. Chem. C* 8 (44) (2020) 15771–15777.
- [80] L. Wang, A. Kutana, X. Zou, B.I. Yakobson, Electro-mechanical anisotropy of phosphorene, *Nanoscale* 7 (21) (2015) 9746–9751.
- [81] F. Mouhat, F.-X. Coudert, Necessary and sufficient elastic stability conditions in various crystal systems, *Phys. Rev. B* 90 (22) (2014) 224104.
- [82] C. Lee, X. Wei, J.W. Kysar, J. Hone, Measurement of the elastic properties and

- intrinsic strength of monolayer graphene, *Science* 321 (5887) (2008) 385–388.
- [83] Q. Wei, X. Peng, Superior mechanical flexibility of phosphorene and few-layer black phosphorus, *Appl. Phys. Lett.* 104 (25) (2014) 251915.
- [84] L. Song, L. Ci, H. Lu, P.B. Sorokin, C. Jin, J. Ni, A.G. Kvashnin, D.G. Kvashnin, J. Lou, B.I. Yakobson, et al., Large scale growth and characterization of atomic hexagonal boron nitride layers, *Nano Lett.* 10 (8) (2010) 3209–3215.
- [85] A. Castellanos-Gomez, M. Poot, G.A. Steele, H.S. Van Der Zant, N. Agrait, G. Rubio-Bollinger, Elastic properties of freely suspended mos2 nanosheets, *Adv. Mater.* 24 (6) (2012) 772–775.
- [86] S. Zhang, J. Zhou, Q. Wang, X. Chen, Y. Kawazoe, P. Jena, Penta-graphene: a new carbon allotrope, *Proc. Natl. Acad. Sci. Unit. States Am.* 112 (8) (2015) 2372–2377.
- [87] J.-W. Jiang, H.S. Park, Negative Poisson's ratio in single-layer black phosphorus, *Nat. Commun.* 5 (1) (2014) 1–7.
- [88] A.J. Mannix, X.-F. Zhou, B. Kiraly, J.D. Wood, D. Alducin, B.D. Myers, X. Liu, B.L. Fisher, U. Santiago, J.R. Guest, et al., Synthesis of borophenes: anisotropic, two-dimensional boron polymorphs, *Science* 350 (6267) (2015) 1513–1516.
- [89] M. Yagmircukardes, H. Sahin, J. Kang, E. Torun, F.M. Peeters, R.T. Senger, Pentagonal monolayer crystals of carbon, boron nitride, and silver azide, *J. Appl. Phys.* 118 (10) (2015) 104303.
- [90] X. Liu, Z. Zhang, Z. Ding, B. Lv, Z. Luo, J.-S. Wang, Z. Gao, Highly anisotropic electronic and mechanical properties of monolayer and bilayer as<sub>2</sub>s<sub>3</sub>, *Appl. Surf. Sci.* 542 (2021) 148665.
- [91] V. Wang, W. Geng, Lattice defects and the mechanical anisotropy of borophene, *J. Phys. Chem. C* 121 (18) (2017) 10224–10232.
- [92] D. Singh, V. Shukla, P.K. Panda, Y.K. Mishra, H.-G. Rubahn, R. Ahuja, Carbon-phosphide monolayer with high carrier mobility and perceptible i-v response for superior gas sensing, *New J. Chem.* 44 (9) (2020) 3777–3785.
- [93] M. Qiao, J. Liu, Y. Wang, Y. Li, Z. Chen, Pdse<sub>0</sub>3 monolayer: promising inorganic 2d photocatalyst for direct overall water splitting without using sacrificial reagents and cocatalysts, *J. Am. Chem. Soc.* 140 (38) (2018) 12256–12262.
- [94] D. Singh, P.K. Panda, N. Khossossi, Y.K. Mishra, A. Ainane, R. Ahuja, Impact of edge structures on interfacial interactions and efficient visible-light photocatalytic activity of metal-semiconductor hybrid 2d materials, *Catal. Sci. Technol.* 10 (10) (2020) 3279–3289.
- [95] K.-A.N. Duerloo, M.T. Ong, E.J. Reed, Intrinsic piezoelectricity in two-dimensional materials, *J. Phys. Chem. Lett.* 3 (19) (2012) 2871–2876.
- [96] Z. Kahraman, A. Kandemir, M. Yagmircukardes, H. Sahin, Single-layer janus-type platinum dichalcogenides and their heterostructures, *J. Phys. Chem. C* 123 (7) (2019) 4549–4557.
- [97] W. Li, J. Li, Piezoelectricity in two-dimensional group-iii monochalcogenides, *Nano Res.* 8 (12) (2015) 3796–3802.
- [98] L. Dong, J. Lou, V.B. Shenoy, Large in-plane and vertical piezoelectricity in janus transition metal dichalcogenides, *ACS Nano* 11 (8) (2017) 8242–8248.
- [99] X. Zhang, Y. Cui, L. Sun, M. Li, J. Du, Y. Huang, Stabilities, and electronic and piezoelectric properties of two-dimensional tin dichalcogenide derived janus monolayers, *J. Mater. Chem. C* 7 (42) (2019) 13203–13210.
- [100] B. Javvaji, B. Mortazavi, X. Zhuang, T. Rabczuk, Exploring tensile piezoelectricity and bending flexoelectricity of diamane monolayers by machine learning, *Carbon* 185 (2021) 558–567.
- [101] A. Reshak, S.A. Khan, S. Auluck, Thermoelectric properties of a single graphene sheet and its derivatives, *J. Mater. Chem. C* 2 (13) (2014) 2346–2352.
- [102] H. Sevincli, C. Sevik, Electronic, phononic, and thermoelectric properties of graphyne sheets, *Appl. Phys. Lett.* 105 (22) (2014) 223108.
- [103] M. Ali, X. Pi, Y. Liu, D. Yang, Electronic and thermoelectric properties of atomically thin c<sub>3</sub>si<sub>3</sub>/c and c<sub>3</sub>ge<sub>3</sub>/c superlattices, *Nanotechnology* 29 (4) (2017), 045402.
- [104] D. Singh, S. Kansara, S.K. Gupta, Y. Sonvane, Single layer of carbon phosphide as an efficient material for optoelectronic devices, *J. Mater. Sci.* 53 (11) (2018) 8314–8327.
- [105] S. Sharma, S. Kumar, U. Schwingenschlögl, Arsenene and antimonene: two-dimensional materials with high thermoelectric figures of merit, *Phys. Rev. Appl.* 8 (4) (2017), 044013.
- [106] B. Zhu, X. Liu, Q. Wang, Y. Qiu, Z. Shu, Z. Guo, Y. Tong, J. Cui, M. Gu, J. He, Realizing record high performance in n-type bi<sub>2</sub>te<sub>3</sub>-based thermoelectric materials, *Energy Environ. Sci.* 13 (7) (2020) 2106–2114.
- [107] D. Kraemer, J. Sui, K. McEnaney, H. Zhao, Q. Jie, Z. Ren, G. Chen, High thermoelectric conversion efficiency of mgagsb-based material with hot-pressed contacts, *Energy Environ. Sci.* 8 (4) (2015) 1299–1308.